# COMPUTER SIMULATION OF THREE-DIMENSIONAL STELLAR SYSTEMS IN CYLINDRICAL COORDINATES

SEUNGHEON SONG, C. W. JUNG, S. Y. KIM

*Department of Physics, Korea Advanced Institute of Science and Technology, Daejon, Korea*

and

YOUNGBO CHOI

*Agency for Defense Development, Daejon, Korea*

(Received 3 September, 1991)

**Abstract.** The $N$-body problem does not have an exact and analytic solution, and computer technique or computer simulation can be a good candidate to solve it. Computing speed in computer simulation is very important. There are many algorithms and computational methods in computer simulation which reduce computer time.

In this report a computer simulation model in a cylindrical coordinate, in which the FACR (Fourier Analysis and Cyclic Reduction) method is used, has been proposed and demonstrated the presence of spiral, barred, and ringed galaxy. The method using a cylindrical grid has good symmetrical properties specially for rotating stellar systems.

## 1. Introduction

The spiral shapes were obtained in the gravitational $N$-body simulations that handled $10^5$ particles moving in a plane under $1/r^2$ forces (Miller *et al.*, 1970; Hohl, 1972; Zang and Hohl, 1978). Theoretical studies have also shown that models of disk galaxies, in which most of stars are in nearly circular motion, are unstable (Kalnajs, 1972; Bardeen, 1975; Hunter, 1979). This instability leads to the formation of a global, intense bar within a few rotation periods. Ostriker and Peebles (1973) have pointed out that the ratio $t$, of the ordered kinetic energy $T$, to the potential energy $W$, must have an absolute value of less than 0.14 if the system is to be stable to the formation of a bar,

$$t = T/|W| \leqq 0.14 .$$

Most of the $N$-body simulation models are usually based on both two- and three-dimensional computer model in a Cartesian coordinate. Lee *et al.* (1990) have pointed out that choice of a suitably boundary condition and the coordinate system which agrees with the symmetrical properties of the dynamical system, speeds up numerical simulation. The newly constructed code for the $N$-body simulation in a polar coordinate was demonstrated to be much better than the code using the rectangular meshes specially for a rotating disk. Examples of potential contour plot in various coordinates and boundary condition have been given to demonstrate the effect of them on the potential calculations in Figure 1. Sellwood (1980) also pointed out that a cylindrical polar coordinate system is perhaps more natural than the Cartesian coordinate system for the

*Astrophysics and Space Science* **193**: 217–234, 1992.

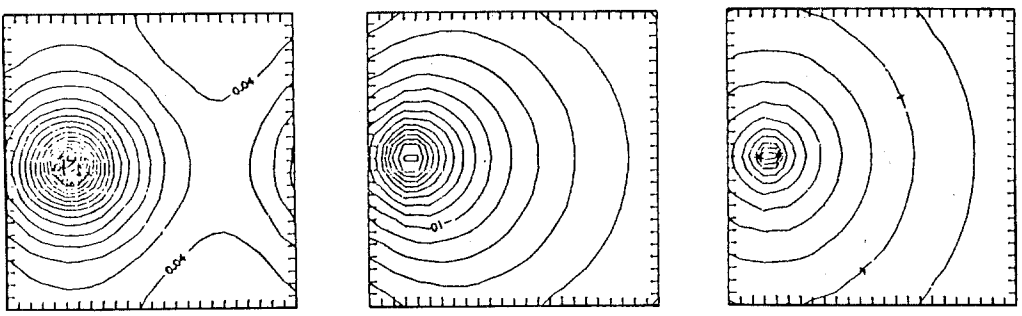


Fig. 1. Results of potential contour plot using (a) periodic boundary condition, (b) constant value boundary condition, and (c) isolated boundary condition.

simulation of a disk galaxy. Miller (1978) has successfully implemented a polar mesh for an infinitesimally thin disk model but the straightforward extension of computer algorithm to three dimensions would turn out to be very expensive.

In this paper the simulation methods of the $N$-body problem in stellar system using cylindrical coordinates will be given and tested. Developing to make computer algorithm for the $N$-body problem, the type of grid should be determined at first. The choice of grid type is dependent on several conditions; boundary conditions, symmetrical properties, computing time, etc.

There are several advantages if a cylindrical grid is used. Most of galaxies have $r - \theta$ symmetry and the density distribution of stars in a stellar system is similar to the Gaussian distribution. Use of cylindrical coordinate system, which can assign dense grid points at small $r$ near the center of the grid system, is good for the $N$-body simulations of stellar system because many grid points can be assigned to dense area near the origin to give a good spatial resolution.

Another advantage is concerned about boundary conditions. It is difficult to use an isolated boundary condition or it takes much time, if a Cartesian grid is used. The FACR (Fourier Analysis and Cyclic Reduction) method has been used for two-dimensional polar coordinates ($r - \theta$) and eigenfunction expansion method has been used for $z$-coordinates for a cylindrical grid.

The computational model, used in this paper, is given and computational methods will be explained briefly in Section 2. In Section 3 simulation model and results are discussed in more detail. Finally in Section 4 a brief discussion and conclusion are given.

## 2. Computational Model

The overall feature of the simulation model developed in this paper is very similar to that of the $N$-body simulation model using a Cartesian coordinate. The $N$-body simulation consists of four different steps: (1) assigning mass of particles into mesh,

(2) solving Poisson's equation on the mesh, (3) computing forces from mesh-defined potential and interpolating forces at particle's position, and (4) pushing particles according to a given force. These four steps and leaf-frog scheme of Newton's equation of motion will be repeated until the end of computer run.

By use of the coordinates other than Cartesian coordinates, Poisson's equation and equation of motion should be modified in a pertinent coordinate system. Thus a new way of numerical analysis should be considered.

Figure 2 shows the cylindrical grid system of our model where $32 \times 32 \times 16$ $(r, \theta, z)$

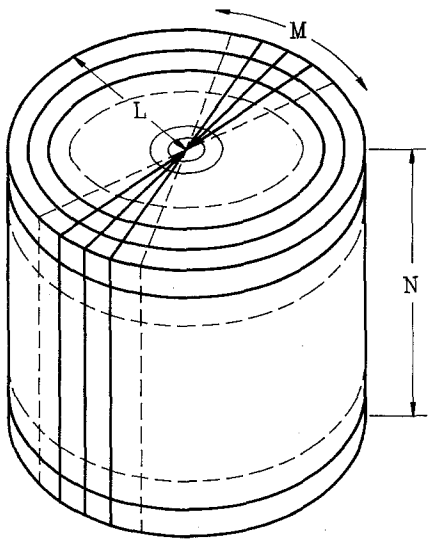


Fig. 2. The grid system of a cylindrical simulation method.

grid has been generated. The value of coordinate $r$ is from 0 to 1, and that of the $z$-coordinate is in the range of 0 to $L$. ($L$ can be given as 0.5 or 2.)

There are many stars in a galaxy. For example, the Milky Way has about $10^{11}$ stars. Since it is impossible to integrate the trajectories of such many stars, the particle-mesh method using superparticles has been used to perform computer simulation (Hohl and Hockney, 1969; Hockney, 1970; Birdsall and Langdon, 1985).

For each iteration the potential will be calculated using Poisson's equation $\nabla^2\phi = 4\pi k\rho$ from given densities assigned at each period. Poisson's equation will be transformed into finite difference equation so that it will be applied into our computer simulation model. Potential and Newton's equation of motion push a particle into its new position and produce its new velocity.

### 2.1. Units

In order to set up an appropriate unit system in the simulation of disk galaxy, unit distance, unit time, and unit mass are determined according to the dimension of the

Milky Way (Kuhn, 1982). The unit distance is determined by the radius of the Milky Way,

$$r_0 = \text{radius of the Galaxy} \simeq 5 \times 10^{20}\ \text{m} = 16\ \text{kpc}\,.$$

In order to determine the relevant time-scales, it is necessary to consider the motion of a star when it is distributed from its circular equilibrium orbit. The unit time is determined by the epicyclic time of the Sun,

$$t_0 = \text{epicyclic time of the Sun} = 6 \times 10^{15}\ \text{s} = 2.5 \times 10^8\ \text{year}\,.$$

The unit mass is determined by the requirement that a superparticle's mass is to be 1,

$$m_0 = \frac{\text{total mass of galaxy}}{\text{number of superparticles}} = \frac{3 \times 10^{41}}{N}\ \text{kg}\,,$$

where $N$ is the number of superparticles in computer simulation model. In the case that $N$ is sufficiently large, gravitational potential satisfies

$$\nabla^2\phi = 4\pi k\rho\,, \tag{1}$$

where $k = Gm_0t_0^2/r_0^3 \simeq 5.8/N$, $G$ is a gravitational constant and $\rho(r, \theta, z)$ is the density distribution function.

## 2.2. Density calculation

In order to obtain gravitational potential, Poisson's equation should be solved. To do that, the mass density at each grid point should be calculated at first. There can be several numerical methods to assign mass density into each grid point. For example, the form factor method or the volume weighting method are most frequently used.

Figure 3 shows how a star's mass is assigned to each grid point. Since the density distribution function should be defined at each grid point to evaluate Poisson's equation

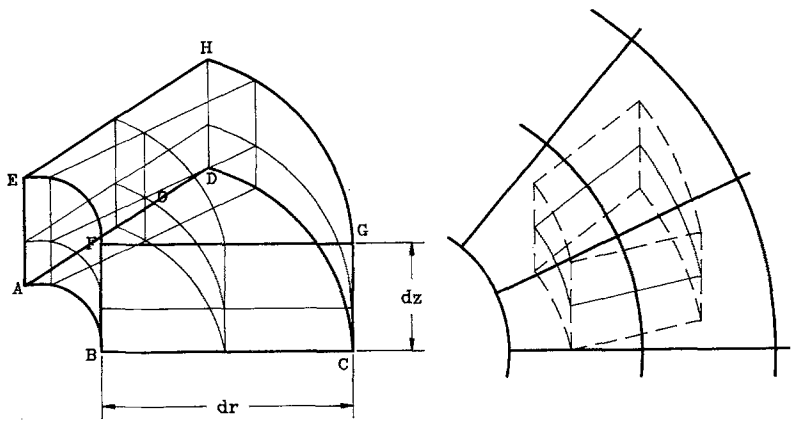


Fig. 3. Volume weighting method.

in a particle mesh method, an appropriate mass is allocated to the nearest grid points with certain ratio. The linear interpolation method has been used in $(r, \theta, z)$ directions. However, either of the two different schemes of the area weighting method in $(r, \theta)$ coordinates are selected from the location of a particle as shown in Figure 4. A star's

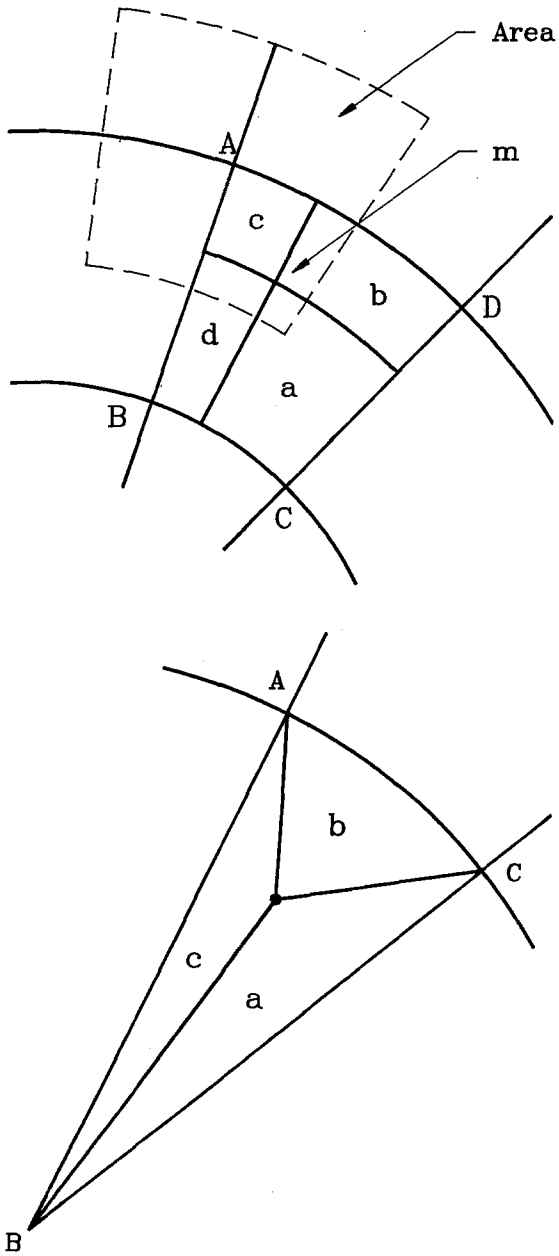


Fig. 4. Area weighting method of $(r, \theta)$ plane at a constant $z$: (a) typical case, (b) near the center.

mass is divided into eight (or six at $r < \Delta r$) pieces and each value is added to the mass density of each grid point, $A$ through $H$ with certain ratio of volume occupied by each point mass as shown in Figure 3.

### 2.3. Potential calculation

The gravitational potential at each grid point can be obtained from the discretized version of Equation (1) and density distribution assigned at each grid. There are several numerical methods available to obtain gravitational potential – for example, FA (Fourier Analysis), CR (Cyclic Reduction), and SOR (Simultaneous Over-Relaxation) methods. In this paper, both FA and CR methods have been used because gravitational potential $\phi(r, \theta, z)$ is assumed to be periodic in $\theta$ and $z$, and have a singular point at $r = 0$. This numerical technique has been numerically implemented in a polar coordinate and is applied to explain gravitational instability of spiral galaxy in a two-dimensional stellar system (Lee *et al.*, 1990). The value of the potential at each boundary point is also required to be given if CR is used.

Equation (1) can be written in terms of $r$, $\theta$, and $z$ (cylindrical coordinate system) as

$$\frac{1}{r}\frac{\partial}{\partial r}\left(r\frac{\partial\phi}{\partial r}\right) + \frac{1}{r^2}\frac{\partial^2\phi}{\partial\theta^2} + \frac{\partial^2\phi}{\partial z^2} = 4\pi k\rho\,. \tag{2}$$

This can be transformed into the finite difference equation as

$$\begin{aligned} &A_{l,m,n}\phi(l,m,n) + B_{l,m,n}\phi(l+1,m,n) + C_{l,m,n}\phi(l-1,m,n) + \\ &\quad + D_{l,m,n}\phi(l,m+1,n) + E_{l,m,n}\phi(l,m-1,n) + F_{l,m,n}\phi(l,m,n+1) + \\ &\quad + G_{l,m,n}\phi(l,m,n-1) = 4\pi k\Delta r^2\Delta\theta^2\Delta\theta^2\rho(l,m,n)\,, \end{aligned} \tag{3}$$

where

$$A_{l,m,n} = -2(\Delta\theta^2\Delta z^2 + \Delta z^2/l^2 + \Delta r^2\Delta\theta^2)\,,$$

$$B_{l,m,n} = \Delta\theta^2\Delta z^2\left(1 + \frac{1}{2l}\right),$$

$$C_{l,m,n} = \Delta\theta^2\Delta z^2\left(1 - \frac{1}{2l}\right),$$

$$D_{l,m,n} = E_{l,m,n} = \Delta z^2/l^2\,,$$

$$F_{l,m,n} = G_{l,m,n} = \Delta r^2\Delta\theta^2\,;$$

$\phi(l, m, n)$ and $\rho(l, m, n)$ are the gravitational potential and density at $r = l\Delta r$, $\theta = m\Delta\theta$, and $z = n\Delta z$, respectively. Note that the coefficients $A_{l,m,n}$ through $G_{l,m,n}$ depend on only the value of $l$.

The DFT (Discrete Fourier Transform) of $\phi$ about $m$ and $n$ indices is given by

$$\bar{\phi}(l,M,N) = \sum_{m=0}^{N_\theta-1}\sum_{n=0}^{N_z-1}\phi(l,m,n)\exp\left[i\left(mM\frac{2\pi}{N_\theta} + nN\frac{2\pi}{N_z}\right)\right]; \tag{4}$$

and the inverse Fourier transform is given by

$$\phi(l, m, n) = \frac{1}{N_\theta} \frac{1}{N_z} \sum_{M=0}^{N_\theta - 1} \sum_{N=0}^{N_z - 1} \bar{\phi}(l, M, N) \exp\left[ -i \left( mM \frac{2\pi}{N_\theta} + nN \frac{2\pi}{N_z} \right) \right]. \tag{5}$$

Trying DFT of Equation (3) about $\theta$- and $z$-coordinates, the following equation is obtained

$$A'_{lMN} \bar{\phi}(l+1, M, N) + B'_{lMN} \bar{\phi}(l, M, N) + C'_{lMN} \bar{\phi}(l-1, M, N) = \\ = 4\pi k \Delta r^2 \Delta\theta^2 \Delta z^2 \bar{\rho}(l, M, N), \tag{6}$$

where

$$A'_{lMN} = \Delta\theta^2 \Delta z^2 \left( 1 + \frac{1}{2l} \right),$$

$$B'_{lMN} = 2 \left( \cos(M\Delta\theta) \frac{\Delta z^2}{l^2} - \frac{\Delta z^2}{l^2} + \cos\left( \frac{2\pi N}{N_z} \right) \Delta\theta^2 \Delta r^2 - \right. \\ \left. - \Delta\theta^2 \Delta r^2 - \Delta\theta^2 \Delta z^2 \right), \tag{7}$$

$$C'_{lMN} = \Delta\theta^2 \Delta z^2 \left( 1 - \frac{1}{2l} \right);$$

$\bar{\phi}$ and $\bar{\rho}$ being discrete Fourier transform of $\phi$ and $\rho$, respectively.

For $l$, $M$, and $N$, all the values of $\bar{\rho}$ are already known from the density distribution assigned at every grid point. The values of $\bar{\phi}$ for $l = 0$ and $N_r$ are specified from the boundary condition. The choice of periodic boundary condition in $z$-coordinate reduces computer time to specify the boundary condition in this simulation model. All the coefficients $A'$, $B'$, and $C'$ in Equation (6) can be calculated. Note that potentials at the boundary can be calculated directly so that $\bar{\phi}(N_r, M, N)$ is obtained.

The cyclic reduction method is applied to the $l$ index for all $M$ and $N$ indices. The potential at all grid points can be determined by the discrete inverse Fourier transform of $\bar{\phi}(l, M, N)$ already obtained through the cyclic reduction method.

### 2.4. Integration of Equation of Motion

By use of the potentials at all grid points, the force which exerts on a particle can be calculated by the interpolation method. From the force on a particle, new velocity and position of it can be calculated by the Runge–Kutta method. Since the potentials are given only on grid points, the interpolation and derivatives of the potential will give a force on the particle. In this paper a linear interpolation scheme is used.

However, a cylindrical grid has a singularity at $r = 0$. Furthermore, $F_\theta$ may have large error when $r$ is small. Thus another interpolation scheme should be considered for $r < \Delta r$. In order to perform an interpolation near $r = 0$, that is $r < \Delta r$, a parabolic

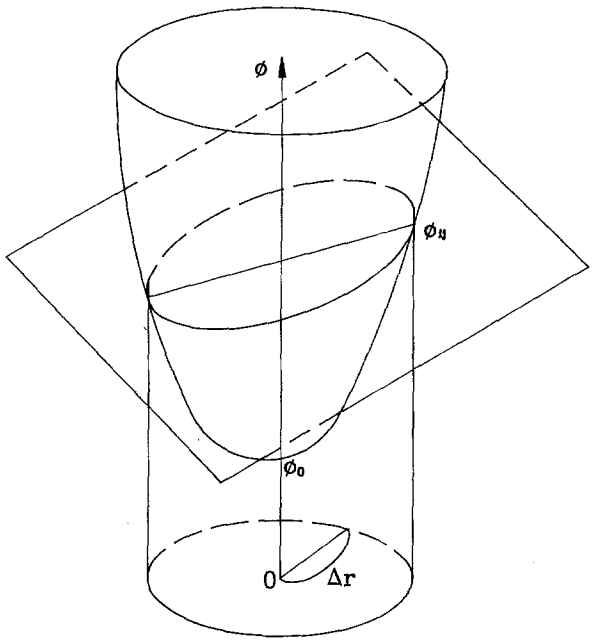


Fig. 5. Interpolation of potential near the center of this simulation model.

function for the $r - \theta$-plane, after linear interpolation being performed for the $z$-axis, is used as in Figure 5. For a given $z$-value, $\phi(l, m, z)$ can be written by

$$\phi(l, m, z) = C + A_m \cos(m\Delta\theta) + B_m \sin(m\Delta\theta), \tag{8}$$

where $A_m$, $B_m$, and $C$ are the corresponding Fourier coefficients, respectively. Then at the neighbourhood of $r = 0$, $\phi$ can be reduced to a paraboloid function which is given by

$$\phi(x, y, z) = (C - \phi_0(z)) \frac{x^2 + y^2}{\Delta r^2} + \frac{A_1}{\Delta r} x + \frac{B_1}{\Delta r} y + \phi_0(z). \tag{9}$$

The components $F_x$, $F_y$, and $F_z$ of a force on a particle can be obtained from the derivatives of the potential given by Equation (9).

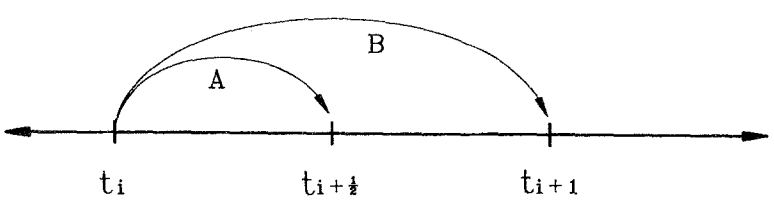


Fig. 6. Second-order Runge–Kutta method.

Now a force acting on a particle at any position can be provided so that the second-order Runge–Kutta method is used to integrate the trajectory of a particle. The equation of motion in a cylindrical coordinate system is given by

$$f_r = \frac{\mathrm{d}v_r}{\mathrm{d}t} - \frac{v_\theta^2}{r}\,, \qquad v_r = \frac{\mathrm{d}r}{\mathrm{d}t}\,,$$

$$f_\theta = 2\,\frac{v_r v_\theta}{r} + \frac{\mathrm{d}v_\theta}{\mathrm{d}t}\,, \qquad v_\theta = r\,\frac{\mathrm{d}\theta}{\mathrm{d}t}\,,$$

$$f_z = \frac{\mathrm{d}v_z}{\mathrm{d}t}\,, \qquad v_z = \frac{\mathrm{d}z}{\mathrm{d}t}\,;$$

and will be integrated using two time steps ($t_{i+1/2}$ and $t_i$) in Figure 6 as

$$v_r' = v_r + \left(f_r + \frac{v_\theta^2}{r}\right)\frac{\Delta t}{2}\,, \qquad r' = r + v_r\,\frac{\Delta t}{2}\,,$$

$$v_\theta' = v_\theta + \left(f_\theta - 2\,\frac{v_r v_\theta}{r}\right)\frac{\Delta t}{2}\,, \qquad \theta' = \theta + \frac{v_\theta}{r}\,\frac{\Delta t}{2}\,,$$

$$v_z' = v_z + f_z\,\frac{\Delta t}{2}\,, \qquad z' = z + v_z\,\frac{\Delta t}{2}\,,$$

and

$$v_r'' = v_r + \left(f_r' + \frac{v'^2}{2}\right)\Delta t\,, \qquad r'' = r + v_r'\,\Delta t\,,$$

$$v_\theta'' = v_\theta + \left(f_\theta' - 2\,\frac{v_r' v_\theta'}{r'}\right)\Delta t\,, \qquad \theta'' = \theta + \frac{v_\theta'}{r'}\,\Delta t\,,$$

$$v_z'' = v_z + f_z'\,\Delta t\,, \qquad z'' = z + v_z'\,\Delta t\,.$$

Since the centrifugal force and Coriolis force are proportional to $r^{-1}$, a large error can be generated at $r < \Delta r$ during the integration of equation of motion. In the region of $r < \Delta r$, cylindrical coordinate system will temporarily be replaced by a Cartesian coordinate system to integrate. The way to integrate the trajectory of a particle in a Cartesian coordinate is similar to that explained above.

## 3. Simulation Results in a Cylindrical Model

The simulation for a disk galaxy is performed by use of Green's function method and by choosing an appropriate boundary condition. The model for a disk galaxy consists of a large number of representative stars (here 5000 ~ 20 000) that are confined to move

in the three-dimensional galactic disk. An $N_r \times N_\theta \times N_z$ (here $32 \times 32 \times 16$) array of cells in a cylindrical coordinate is superposed over the volume of the disk for the purpose of calculating gravitational potential. At the center of each cell a mass density is defined which is given by the ratio between the number of stars and the volume of that cell.

The system to be investigated is a disk with a Gaussian volume mass density

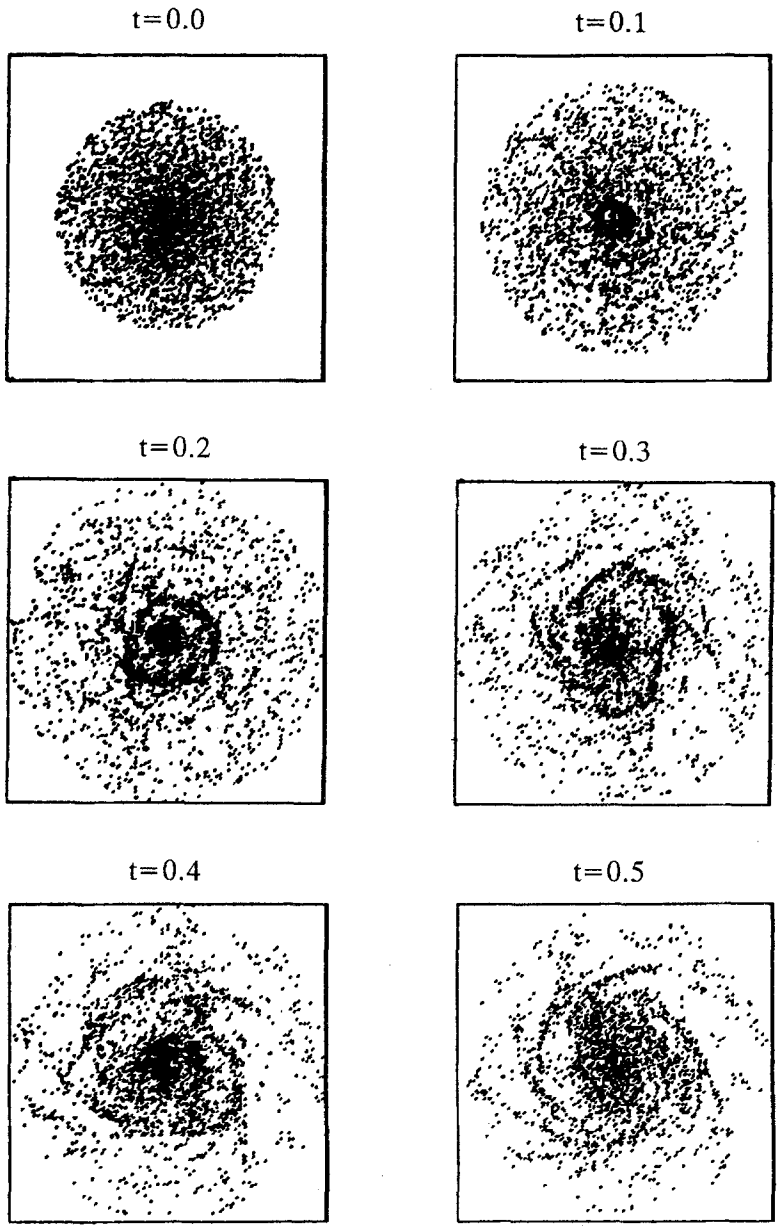


Fig. 7. Evolution of the spiral galaxy.

distribution given by

$$\rho(r, \theta, z) = \rho(0, 0, 0) \exp\left[ -\alpha(r/r_0)^2 - \beta\left(z - \frac{L}{2}\right)^2\right], \tag{10}$$

where $r_0$ is a cut-off radius, $\alpha$ and $\beta$ are suitable coefficients, respectively. Furthermore, the range of $z$ is restricted by

$$\left(\frac{L}{2}\right)(1 - \delta \exp(-r/r_0)^2)) < z < \left(\frac{L}{2}\right)(1 + \delta \exp(-(r/r_0)^2)) \tag{11}$$

to give an initial distribution of the disk galaxy.

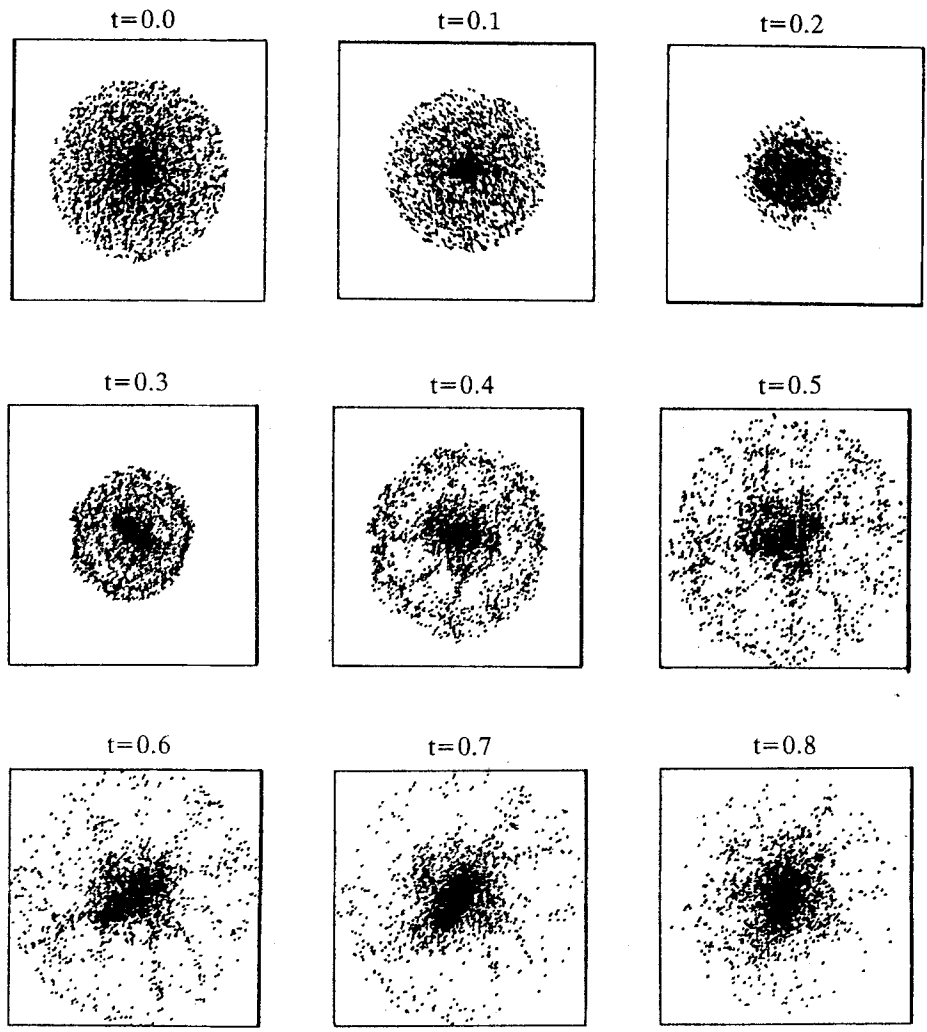


Fig. 8. Evolution of the barred galaxy.

The rotational velocity required to balance a cold disk with Gaussian volume density was given by

$$v_\theta = \varepsilon v_s ,$$

where $v_s$ is numerically calculated under the condition that gravitational attraction is equal to centrifugal force at each particle's location. Note that the numerically evaluated value of $v_s$ is quite similar to that given by Toomre (1963). The choice of coefficient $\varepsilon$ is given by

$$0.3 \leqq \varepsilon \leqq 2.0 .$$

To stabilize an axisymmetric disturbance anywhere in the hot disk, an appropriate effect of velocity dispersion is added as

$$v_r = \text{gaussian} , \qquad v_\theta = \langle v_\theta \rangle + \text{gaussian} , \qquad v_z = \text{gaussian} .$$

In order to investigate the effect due to the halo component, particles of the halo component are uniformly distributed inside a suitably defined sphere. With a suitable

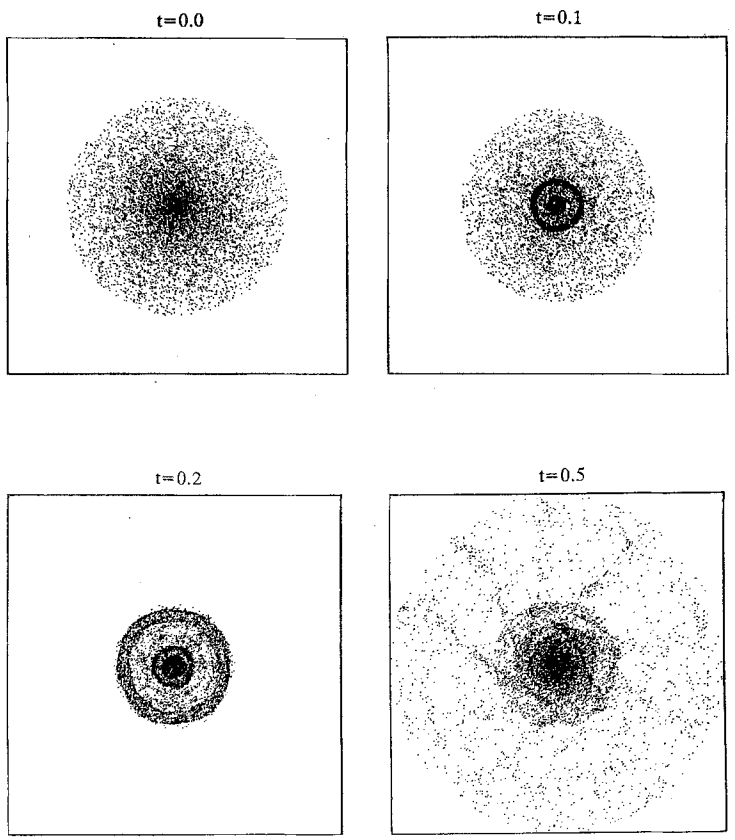


Fig. 9. Evolution of the ringed galaxy.

choice of the above-mentioned initial condition, various simulations are performed to show the presence of spiral, ringed, barred, and irregular galaxies which are frequently observed.

Figure 7 indicates a two-dimensional projected plot $(r, \theta)$ which shows clear pattern of the spiral galaxy. The initial condition used in this simulation is given by $\varepsilon = 0.5$, $L = 0.5$, $N = 5000$, $\alpha = 1$, $\beta = 1$, $\gamma = 0$, $\delta = 0.5$, $r_0 = 0.7$, and $\Delta t$(time step) = 0.0005, respectively. Initially a clear pattern of collapse towards the center of the galaxy is observed because of strong attractive force due to gravitation. As time goes on, the pattern of nuclear and inner ring appears due to the instantaneous equilibrium between rotation and gravitation. Existence and observation of the ringed galaxy has already been confirmed by Buta (1988). Later ring structure disappears and rotating spiral pattern has been observed. This may happen due to the fact that any minor leading disturbance unwinds and is then swing amplified into a short trailing disturbance which propagates through the disk center and emerges as a short leading disturbance.

Figure 8 indicates a two-dimensional projected plot $(r, \theta)$ which shows the evolution into rotating barred galaxy. The initial condition used in this simulation is given by

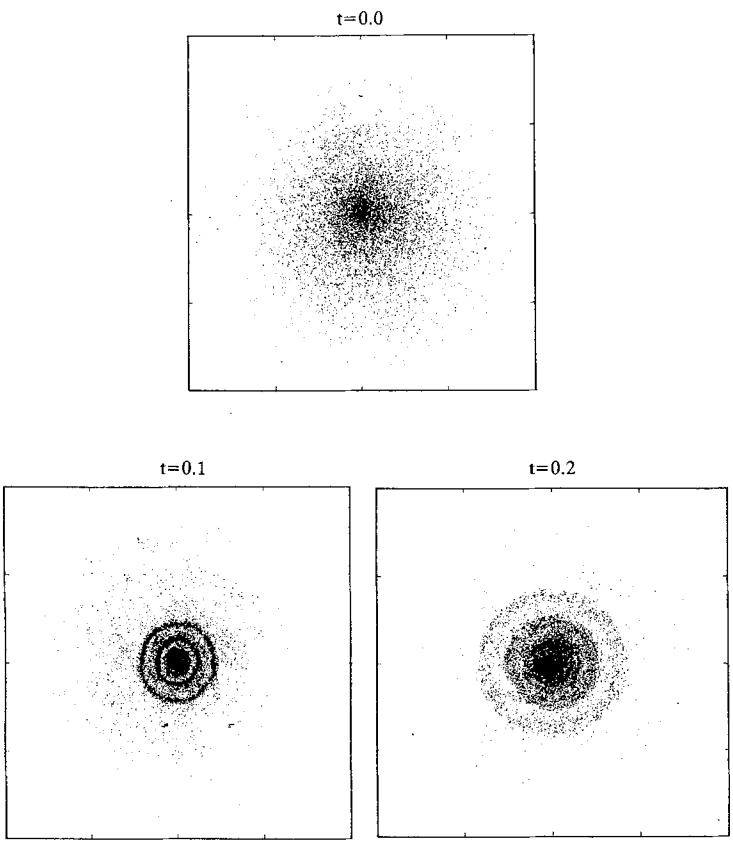


Fig. 10. Evolution of the ringed galaxy with the halo component.

$\varepsilon = 0.5$, $L = 0.5$, $N = 10000$, $\alpha = 1$, $\beta = 2.303$, $\gamma = 2.303$, $\delta = 0.5$, $r_0 = 0.5$, and $\Delta t = 0.001$, respectively. The system is unstable against relatively slowly growing nonaxisymmetric disturbances so that a bar-shaped structure has been clearly produced.

Figure 9 shows a two-dimensional projected plot $(r, \theta)$ which points out the evolution of the ringed galaxy. The initial condition used in this simulation is $\varepsilon = 0.5$, $L = 2$, $N = 20000$, $\alpha = 1.05$, $\beta = 1.05$, $\gamma = 1.05$, $\delta = 0.1$, $r_0 = 0.65$, and $\Delta t = 0.001$, respectively. In de Vaucouleur's classification there are three major ring types: inner rings, which occur in the inner regions but outside the bulge; outer rings, which are usually

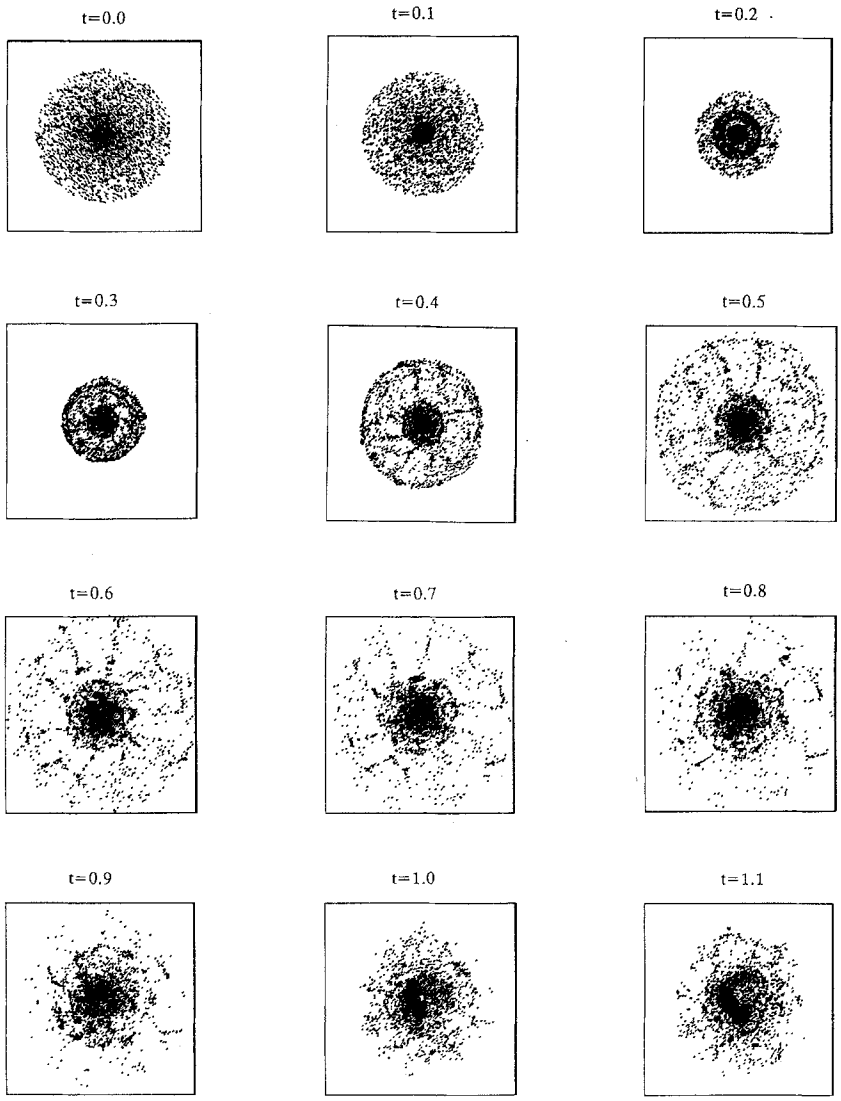


Fig. 11. Evolution of the irregular galaxy.

low surface brightness structures in the outer parts of many early-type disk galaxies; and nuclear rings, which are almost exclusively found in bulges. The simulation shows only the existence of nuclear and the inner ringed galaxy. The inner ring is especially well-defined and conspicuous, the outer ring is very faint. Rings in ordinary galaxies may be related to orbital resonances with a bar, oval distortion, or density wave. The probable association between rings and resonances has long been studied (Lin, 1971). Further dynamical modelling and observations of this kind of galaxies would, therefore, be worthwhile.

In order to investigate the effect of the halo component on the ring galaxy, the following initial condition has been used: $\varepsilon = 1.4$, $L = 1.0$, $N = 20000$, $\alpha = 4.61$,

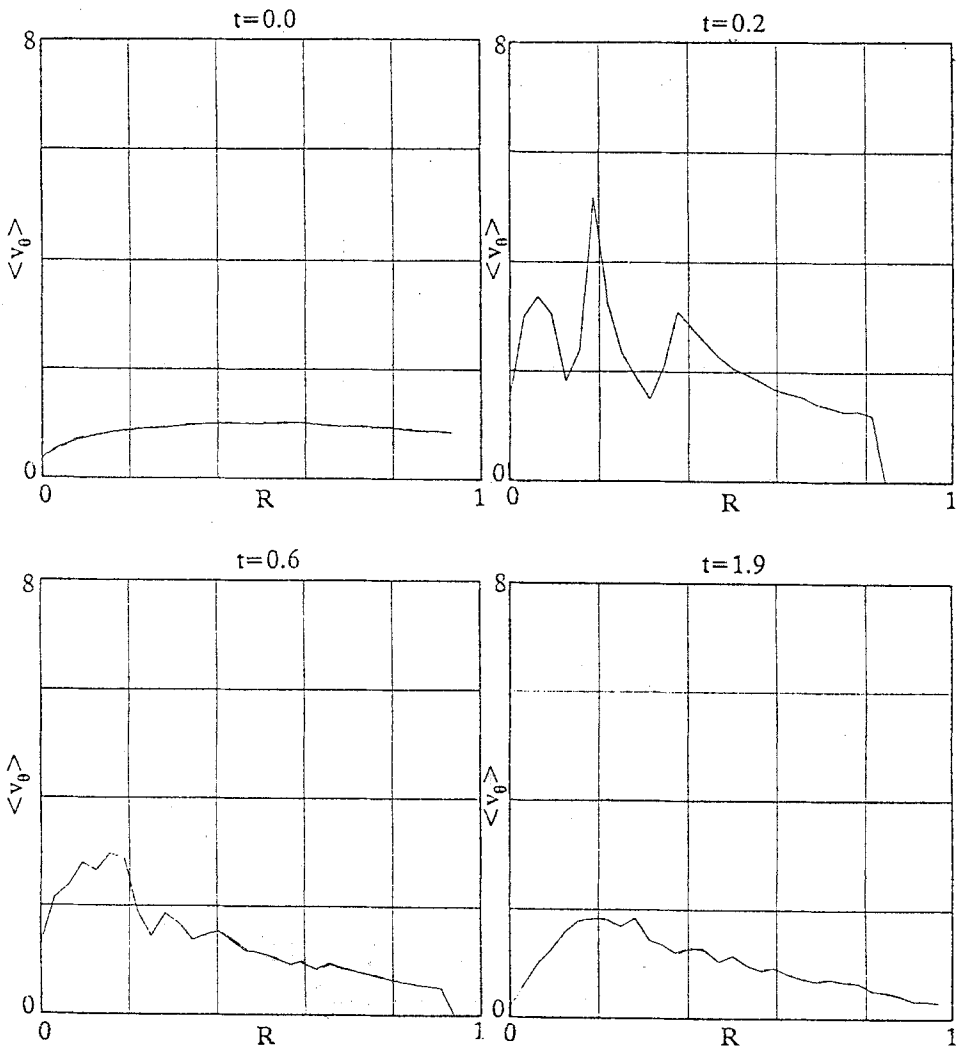


Fig. 12. Mean rotational velocity $\langle v_\theta \rangle$ profile.

$\beta = 4.61$, $\gamma = 4.61$, $\delta = 0.5$, $r_0 = 1$, and $\Delta t = 0.0005$, respectively. The number of particles in the halo component is chosen as 3000, and they are uniformly distributed inside the sphere of radius 0.4. Figure 10 shows the clear pattern of nuclear, inner, and outer rings. Note that the presence of small structure inside the nuclear ring is also detected.

Figure 11 shows the evolution of an irregular galaxy. The initial condition used in this simulation is $\varepsilon = 0.3$, $L = 0.5$, $N = 20000$, $\alpha = \beta = 0.92$, $\gamma = 2.30$, $\delta = 0.15$, $r_0 = 0.7$, and $\Delta t = 0.005$. As time goes on, collapse towards the center or expansion from the center of the galaxy continuously occur one after another and finally more than 50% of the stars in the galaxy begins to shift form the center and to rotate, forming irregular pattern. This phenomenon is observed in the Large Magellanic Clouds.

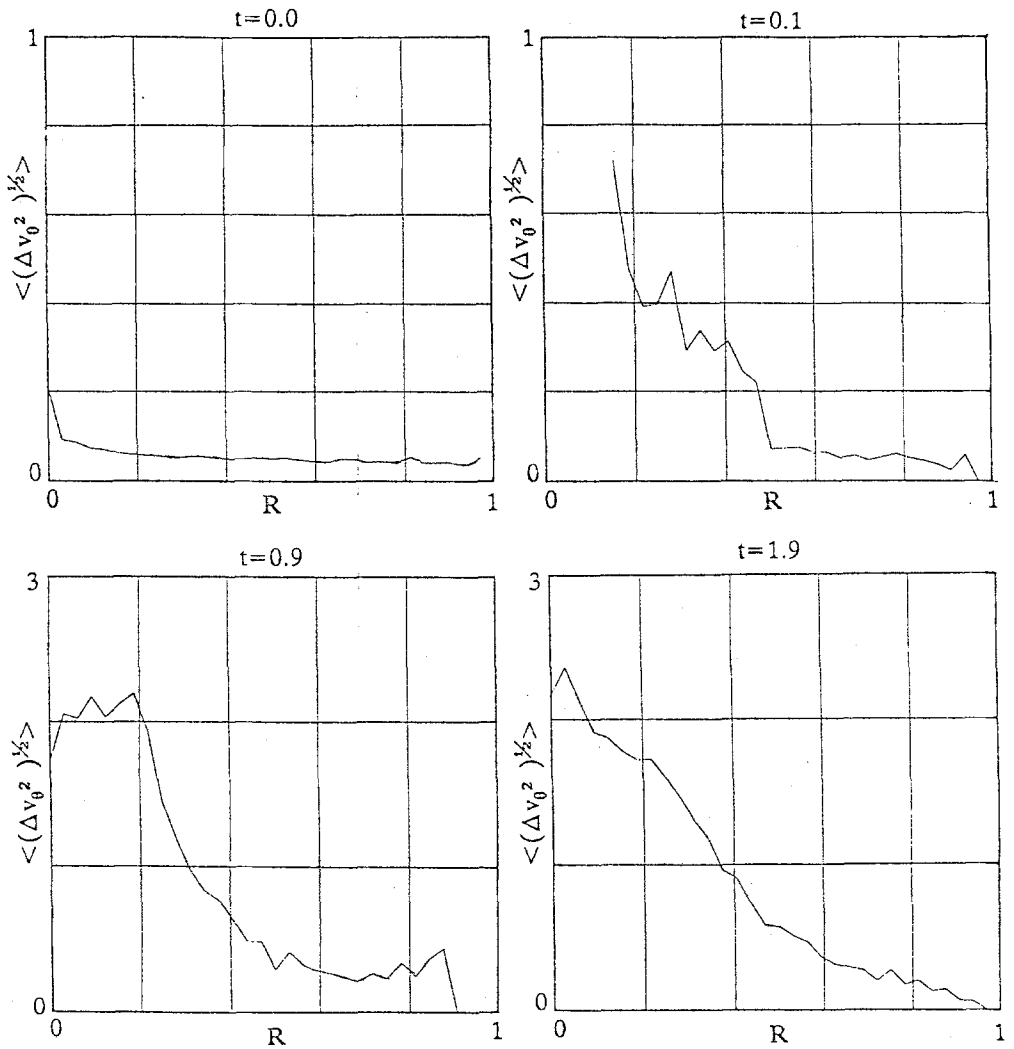


Fig. 13. Mean rotational velocity dispersion $\langle(\Delta v_\theta)^2\rangle^{1/2}$ profile.

Figure 12 shows the mean circular velocity profile of stars versus radial distance $r$ for a spiral galaxy. The time history $\langle v_\theta \rangle$ shows that the mean velocity is greatly reduced for both small and large values of $r$ while it increases for intermediate values. The sharp peak of $\langle v_\theta \rangle$ for the intermediate value of $r$ at $t = 0.2$ may be related to the presence of inner ring at early stage of the rotating disk galaxy. The sharp peak disappears leading to flat velocity distribution with radial distance due to the relaxation process.

It is of interest to obtain the values of the azimuthal velocity dispersion $\langle (\Delta v_\theta)^2 \rangle^{1/2}$. The time history of $\langle (\Delta v_\theta)^2 \rangle^{1/2}$ shows that the azimuthal velocity dispersion sharply increases at small values of $r$, as in Figure 13. A purely rotating stellar disk is stabilized

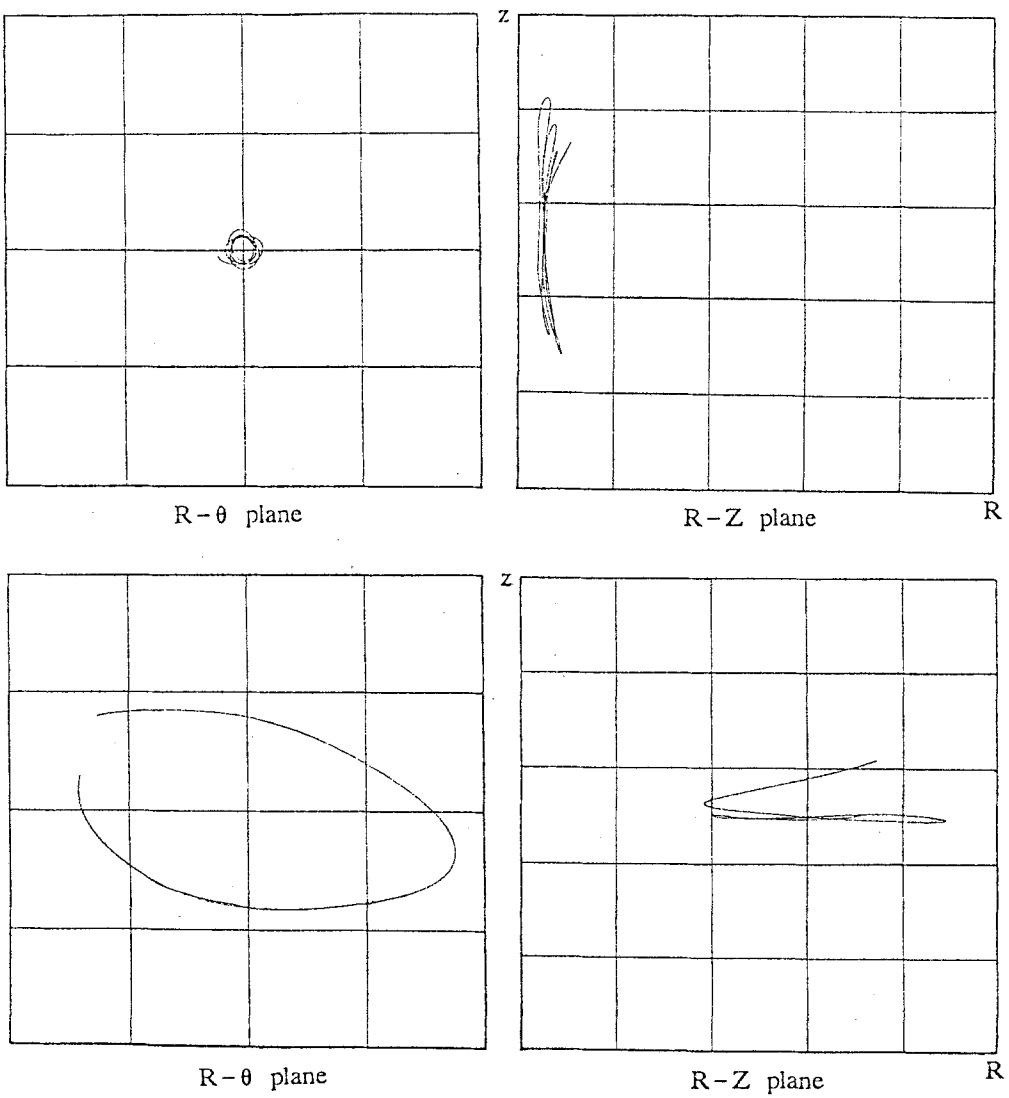


Fig. 14. Orbits of two individual particles.

only with very high-velocity dispersions such that more than 50% of the total kinetic energy is in random motion with the remaining kinetic energy in rotation. Note also that the bar-forming instability is stabilized by the halo component.

Two individual star orbits taken at random from the 20 000 stars in the disk galaxy are shown in Figure 14. The orbits are plotted by simply connecting the position of a star at each time step. The orbits indicate that stars initially near the center of the disk have a tendency to become trapped in even tighter orbits in $(r, \theta)$-coordinates as the central mass density increases. However, in $(r, z)$-coordinates it can go freely in the direction of $z$-coordinates. Stars further out have a tendency to escape from the system in $(r, \theta)$-coordinates. The frequency of oscillations in the star orbits is similar to that deduced from epicyclic theory.

## 4. Conclusions

The simulation code newly constructed for a three-dimensional cylindrical computer model has been tested using a rather simple initial condition. The important consideration of the simulation code lies in the speed as well as accuracy of the simulation model. The code developed here may be useful for a simulation of a system with rotational symmetry. Further investigation of the disk galaxy simulation will be proceeded.

## Acknowledgements

This research has been partly supported by KOSEF grant and Cray Research grant.

## References

Bardeen, J. M.: 1975, *Proc. IAU Symp.* **69**, 297.
Birdsall, C. K. and Langdon, A. B.: 1985, *Plasma Physics via Computer Simulation*, McGraw-Hill Co., New York.
Buta, R.: 1988, *Astrophys. J. Suppl.* **66**, 233.
Hockney, R. W.: 1970, *Methods in Computational Physics*, Vol. 9, Academic Press, New York.
Hohl, F.: 1972, *J. Comput. Phys.* **9**, 10.
Hohl, F. and Hockney, R. W.: 1969, *J. Comput. Phys.* **4**, 306.
Hunter, C.: 1979, *Astrophys. J.* **227**, 73.
Kalnajs, A. J.: 1972, *Astrophys. J.* **175**, 63.
Kuhn, L.: 1982, *The Milky Way*, John Wiley and Sons, New York.
Lee, G. H., Kim, S. Y., Lee, T. W., and Kim, K. S.: 1990, *New Physics* **30**, 602 (Korean edition).
Lin, C. C.: 1971, *Highlights Astron.* **2**, 88.
Miller, R. H.: 1978, *Astrophys. J.* **223**, 811.
Miller, R. H., Prendergast, K. H., and Quirk, W. J.: 1970, *Astrophys. J.* **161**, 903.
Ostriker, J. P. and Peebles, P. J. E.: 1973, *Astrophys. J.* **186**, 467.
Sellwood, J. A.: 1980, *Astron. Astrophys.* **89**, 296.
Toomre, A.: 1963, *Astrophys. J.* **138**, 385.
Zang, T. A. and Hohl, F.: 1978, *Astrophys. J.* **226**, 521.